ACS APPLIED NANO MATERIALS

Article

Cite This: ACS Appl. Nano Mater. 2019, 2, 100−108

www.acsanm.org

Refractory Vertically Aligned Carbon Nanotube−Boron Nitride Nanocomposites for Scalable Electrical Anisotropic Interconnects

Qi Ming Zou,[†] Lei Min Deng,[†,∥] Pei Xun Fan,[*,†] Da Wei Li,[†] Chen Fei Zhang,[†] Li Sha Fan,[†] Lan Jiang,[£] Jean-Francois Silvain,[§] and Yong Feng Lu[*,†]

[†]Department of Electrical and Computer Engineering, University of Nebraska—Lincoln, Lincoln, Nebraska 68588-0511, United States

[£]School of Mechanical Engineering, Beijing Institute of Technology, Beijing 100081, China

[§]Institut de Chimie de la Matière Condensée de Bordeaux, Avenue du Docteur Albert Schweitzer, Cedex F-33608 Pessac, France

[∥]Wuhan National Laboratory for Optoelectronics, Huazhong University of Science and Technology, Wuhan 430074, China

Supporting Information

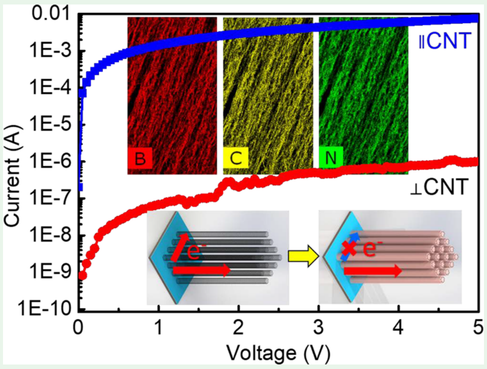

ABSTRACT: Traditional metal interconnect technology faces several challenges when scaling down, such as electromigration and poisoning. Carbon nanotubes (CNTs) have been introduced in an attempt to solve these problems while providing on par performance. However, unexpected issues, such as great difficulty in manufacturing perfectly aligned CNTs and the undesired current leakage caused by electron percolation, still exist. In this work, we present novel vertically aligned CNT (VACNT)-based nanocomposites utilizing hexagonal boron nitride (h-BN) as intertube insulating/shielding layers that can be prepared in a scalable and controllable fashion. This composite material inherits the full advantages of the directional conductivity of VACNTs which are strongly enhanced by the intertube h-BN layer and demonstrate excellent electrical anisotropy. This composite material achieves conductivities of 1060.43 and 4.43 S m^{-1} along the directions parallel and perpendicular to the VACNTs, respectively, while the previously reported electrical conductivity of CNT−polymer and CNT−ceramic counterparts are well below 10^{-3} S m^{-1} isotropically. Because of its refractory ability, the h-BN layer can also protect the prepared nanocomposites from harsh oxidation and erosion, showing ultrahigh stability up to 1400 °C. These results reflect a giant step toward a simple, turnkey solution to an advanced CNT-based composite material for future electrical interconnect applications.

KEYWORDS: *anisotropic, ceramic nanocomposites, vertically aligned carbon nanotube, electrical interconnects, boron nitride*

1. INTRODUCTION

Modern interconnect technology was introduced into the fabrication of printed circuit boards (PCBs) and very-large-scale integration (VLSI) at least two decades ago.[1−5] It allowed PCBs to be designed with much higher routing density[6] and revolutionized the VLSI industry by significantly increasing the performance of chips.[7] As feature sizes continuously shrink, interconnect technology demands much denser routing to decrease costs and avoid reliability risks.[6] While copper (Cu) interconnects are dominating the market, they require barrier layers or special alloys to prevent poisoning when ramping up the routing density.[1] In addition, Cu interconnects suffer electromigration (EM) which worsens when the current density increases.[8]

Carbon nanotubes (CNTs) have recently been recognized as a promising alternative to Cu interconnects.[9,10] It has been suggested that CNTs are the interconnect material of the future[11] based on their outstanding electrical properties as well as extraordinary failure current densities ($>10^9$ A cm^{-2}).[9,10,12−15] In addition, CNTs have the ability to carry huge current density without heat sinks because of their exceptional thermal conductivity.[16,17] However, great difficulty exists in manufacturing perfectly aligned CNTs, which are beneficial for minimizing the conducting resistance.[18,19] When stacking clustered CNTs, the intertube conduction becomes significant due to electron percolation, causing current leakage toward unwanted directions.[20] Consequently, CNT−dielectric composite systems have been introduced to manipulate the percolation by fine controlling the electrical percolation threshold (EPT) to prevent intertube conducting behavior, at the expense of high electrical conductivity, however, when compared to bare CNT networks. In such systems, consisting of a mix of dielectric and conductive materials, the formation of conductive pathways in the form of clusters of aligned CNTs inside the matrix is governed by classical percolation theories.[21,22] The conductivity of CNT−dielectric composite

Received: September 30, 2018
Accepted: December 31, 2018
Published: January 4, 2019

DOI: 10.1021/acsanm.8b01727
ACS Appl. Nano Mater. 2019, 2, 100−108

systems depends upon the alignment of nanotubes, with the highest conductivity being obtained via highly aligned CNTs.[18] On this basis, a promising solution for addressing all of the stated issues is to combine vertically aligned carbon nanotubes (VACNTs) with appropriate dielectric materials.

As a thermally and chemically resistant refractory compound of boron (B) and nitrogen (N), boron nitride (BN) came to our attention. It exists in various crystalline forms that are isoelectronic to a similarly structured carbon lattice.[23] Among those forms, hexagonal boron nitride (h-BN) demonstrates excellent anticorrosion ability,[24] thermal stability,[25] and, as a wide-bandgap semiconductor material, a decent dielectric property.[26] However, the fabrication of VACNT-BN remains a huge challenge. As we know, the average intertube distance in VACNT arrays is <10 nm, which greatly limits the infiltration of the majority of materials into the VACNT array.[27,28] Although thermal chemical vapor deposition (CVD)[28−30] and atomic layer deposition (ALD)[31] have been reported to be effective in regard to the infiltration of materials into dense VACNT arrays, successful preparation of VACNT-BN nanocomposites with electrical anisotropy has rarely been realized.

In this work, we developed an efficient approach to the controllable fabrication of VACNT-BN nanocomposites, which utilized VACNTs as a conductive network and h-BN as an intertube shielding layer, via a single-step CVD process. Vertically aligned carbon nanotubes, rather than other carbon (C) nanomaterials, were chosen as the conducting framework due to their highly aligned structure which guarantees the conductive pathway after the infiltration of h-BN into the matrices and minimizes the thermal stress at elevated temperatures.[17] The as-prepared VACNT-BN nanocomposites exhibited highly anisotropic conductivity in the network, the mechanism behind which was studied and attributed to the different electrical percolation thresholds in different directions as a nature of the VACNT-BN nanocomposites. The nanocomposites also have excellent high-temperature antioxidative ability (up to 1400 °C) and erosion resistance, suggesting that the prepared VACNT-BN nanocomposites have great potential for next-generation electrical interconnects, but much more potential is yet to be explored.

2. METHODS

Fabrication of Ultralong VACNTs via CVD. Ultralong VACNTs were fabricated in a similar fashion as reported previously.[28] The growth of VACNTs was performed in a two-zone CVD furnace (MTI Corporation, OTF-1200X) after appropriate catalysts were sputtered onto the substrate. Two different types of VACNT samples were prepared: VACNT films and cuboid-patterned VACNTs.

Fabrication of VACNT-BN Nanocomposites. VACNT-BN nanocomposites were prepared via CVD. The VACNT samples were placed inside a tube furnace with customized gas inlets and were heated in an ammonia flow until 1100 °C was reached. Then, boron trifluoride was introduced into the chamber over a time period as long as 180 min. During the BN deposition, the chamber pressure was maintained at ~2.3 Torr.

Fabrication of VACNT-BN Electrical Conductivity Test Benches and *I*−*V* Measurements. VACNT-BN samples were thinned and lifted out of the bulk matrices via FIB (FEI, Helios NanoLab 660). Electrode patterns were prepared via photolithography (SUSS MicroTec Group, MJB4 Mask Aligner), and Au was then sputtered by a magnetron sputtering system (AJA International, Inc., ATC-Orion 5 UHV) to obtain Au electrodes. The VACNT-BN lifted out were then transferred onto the Au electrodes. The *I*−*V* characteristics were measured by a probe station (Cascade MPS 150) and a semiconductor parameter analyzer (Agilent 4155C) at room temperature.

High-Temperature Antioxidative Ability and Thermal Stability Test. For antioxidative ability testing, the as-prepared h-BN film and VACNT-BN nanocomposites were oxidized in a muffle furnace (Thermolyne Benchtop 1100 °C) at different temperatures until 1100 °C. Further oxidation from 1100 to 1400 °C was performed in a tube furnace (MTI Corporation, GSL-1500X-RTP50), with an oxygen partial pressure of 100 mTorr. High-temperature gas erosion resistance of VACNT-BN was performed by an oxyacetylene torch for as long as 126 min (Figure S16, Supporting Information).

Characterization. Raman spectral analysis of the samples was performed in a micro-Raman system (Renishaw, inVia Plus). A 514 nm Ar^+ laser with a power of ~3 mW was used to excite the Raman scattering. Raman spectra and mapping were then collected through a 50× objective lens with an accumulated time of 10 s at each position. Scanning electron microscopy (FEI, Helios NanoLab 660) was used to study the morphologies of the as-prepared VACNT-BN nanocomposites. Energy-dispersive X-ray analysis was performed via this SEM system as well. Transmission electron microscopy (FEI, Tecnai Osiris S/TEM) was used to study the nanostructures of the grown BN and VACNT-BN samples. Energy-dispersive X-ray, EELS, and HAADF analyses were also performed via this scanning TEM system.

3. RESULTS AND DISCUSSION

3.1. Design and Fabrication. *3.1.1. Growth of Thick Boron Nitride Layers.* In this study, thick boron nitride films were prepared via CVD. Hexagonal boron nitride film as thick as 11.8 μm (Figure S1) was successfully obtained in a fashion similar to the one reported previously,[32] with a growth time of 180 min, corresponding to a fast growth rate of ~4 μm/h. Interestingly, two different kinds of h-BN structures can be distinguished from the cross-sectional scanning electron microscopy (SEM) image shown in Figure S1b. To chemically examine the h-BN film grown, cross-sectional Raman mapping was obtained and is shown in Figure S2 to provide more structural and quality information about the as-grown, thick h-BN film. The Raman mapping of peak intensity, peak position, and peak width of the as-grown h-BN were compared (Figure S2c−h). The peak intensity was strong in the top section (layered) of the h-BN and was slightly lower in the bottom section (particle-like) of h-BN. However, there was not much difference in the peak position and width of the E_{2g} band across the cross section, suggesting an overall uniform distribution of quality.[33] To further confirm the crystal structure of these two different layers, a cross-sectional transmission electron microscopy (TEM) sample ~25 nm thick was prepared via focused ion beam (FIB), shown in Figure S3. As can be seen, the top BN layer shows a highly oriented, layered structure, as typical h-BN. On the contrary, the bottom BN layer contained many different polycrystalline orientations, which was confirmed to be amorphous BN. The electron energy loss spectroscopy (EELS) spectrum, shown in Figure S3e, further confirms the BN structure.

3.1.2. Controlled Growth of Boron Nitride on Vertically Aligned Carbon Nanotubes. We applied the same h-BN growth technique directly onto VACNTs instead of silicon dioxide/silicon (SiO_2/Si). As previously reported, the infiltration of materials into dense VACNT arrays is extremely challenging, and the thermal CVD system was fine-tuned to ensure a homogeneous dispersion of h-BN inside the VACNT arrays.[28] Figure 1a illustrates the controlled fabrication process of VACNT-BN nanocomposites. To fabricate VACNT-BN samples, both VACNT films of different thicknesses (Figure 1a) and cuboid-patterned VACNTs (Figure 1b,c) were

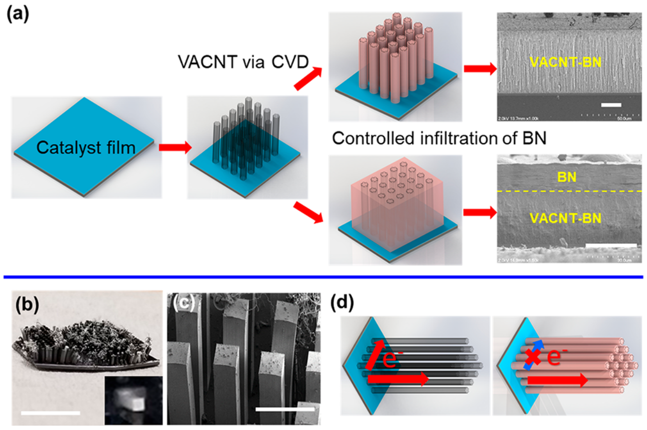

Figure 1. Illustration of controlled fabrication process and electron percolation mechanism. (a) The controlled fabrication process of VACNT-BN. Two cross-sectional SEM images demonstrate two different types of VACNT-BN film samples. (b) Optical image and (c) SEM image of cuboid-patterned VACNT-BN sample. The inset in (b) shows one single magnified VACNT-BN cuboid. (d) Different electron percolation conditions in VACNT and VACNT-BN. Scale bars for (a) 20 μm, (b) 1 cm, and (c) 50 μm.

prepared for the h-BN infiltration. Optimized h-BN growth parameters were used for the infiltration, and the corresponding X-ray diffraction (XRD) results for VACNTs, h-BN film, and VACNT-BN (shown in Figure S4) were used to confirm the composite structure. As can be seen, both h-BN film and VACNT-BN exhibited a main feature of (002) while only VACNT-BN exhibits (004). It is reported that the (002) plane of h-BN exhibits similar properties of a graphene-like plane.[34] While the (004) plane of h-BN is parallel to the (002) plane, the XRD intensity of these two planes can be largely different due to different facets that are exposed in the crystals.[35] This indicates that the crystal alignment of h-BN film and that of VACNT-BN are different, which could be caused by a much more complicated surface condition of VACNTs for BN to grow.

The well-controlled growth of VACNT-BN yielded short (Figure S5) and ultralong (Figures S6 and S7) VACNT-BN nanocomposites. Figure S5 is a cross-sectional SEM image of an as-grown, short VACNT-BN sample. An excessive layer of h-BN can be seen above the lower VACNT-BN section. The VACNTs were heavily covered by h-BN as the fiber structures visually became much thicker. Figures S6 and S7 demonstrate the uniformity of the ultralong VACNT-BN nanocomposites along all directions. As an example, a 1.3 mm long VACNT-BN cuboid was cut in half, and the cross-sectional SEM images for vertical (Figure S6) and horizontal (Figure S7) directions of the sample are presented. As shown in these results, the uniformity in macroscale turns out to be excellent.

3.1.3. Controlled Intertube Conduction Manner. In our VACNT-BN system, the composite mixture was highly oriented by utilizing the VACNT as a template. Without insulating layers outside the VACNTs, current flowed along the direction of the VACNTs and intertube at the same time due to electron percolation (illustration Figure 1d). To achieve highly anisotropic conductivity, we engineered the VACNT-BN nanocomposites, based on the dielectric nature of h-BN. Dense VACNT arrays were used as the conducting network and building template, into which we infiltrated BN in a controlled manner. Hexagonal boron nitride served as an intertube shielding layer, increasing the electron percolation threshold of the VACNTs while maintaining the pristine conducting ability along the direction of the VACNTs.

3.2. Structural and Chemical Characterization.

Although the graphene-like structure of the wall of VACNTs can act as a template for the nucleation of h-BN, achieving a stable and functional combination of these two materials remains a great challenge.[29,36−39] To explore this matter, we first looked into the structure, in macroscale, of the VACNT-BN nanocomposites. Cross-sectional SEM images of them are presented in Figure 2. During the growth of h-BN, gas feedstocks first infiltrated into the VACNT array, forming h-BN layers which eventually accumulated on the top surface, resulting in the formation of a thick h-BN layer on top. As can be seen in Figure 2a,b, the h-BN layer on top exhibited a layered structure while the VACNT-BN region maintained its original vertically aligned feature (Figure 2d). The magnified SEM image (Figure 2b) gives a clearer view of the layered h-BN structure. Different boundaries are outlined by the yellow dashed lines, indicating the evolution in size of h-BN layers, from small fractions to larger plains. The small fractions are considered to be the consequence of direct growth on the top surface of the VACNT array, which was very rough. In addition, a clear boundary of VACNT-BN and h-BN regions can be identified (Figure 2c).

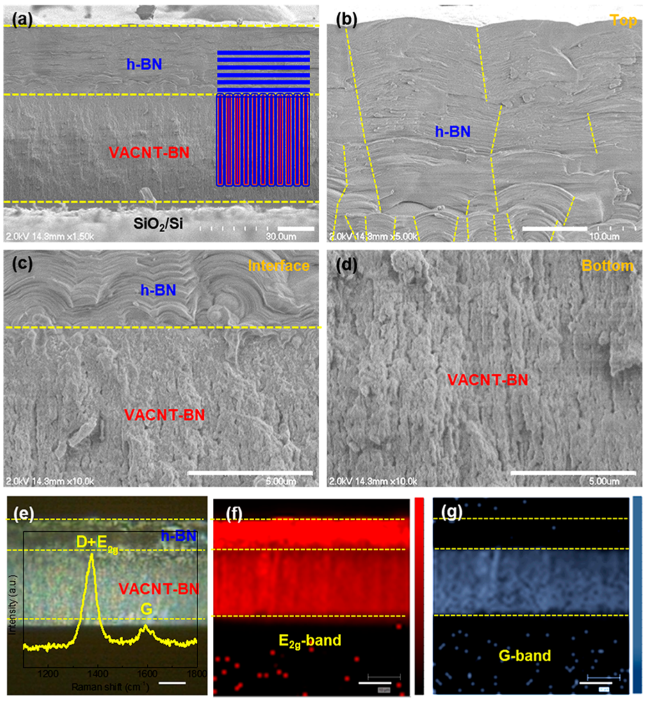

Figure 2. Microscale structural and chemical analysis of prepared VACNT-BN nanocomposites. (a) Low magnification cross-sectional SEM images of VACNT-BN. Scale bar: 10 μm. (b−d) High magnification cross-sectional SEM images corresponding to the top, interfacial, and bottom area of (a), respectively. Scale bar: 5 μm. (e) Optical microscopic image of the sample. (f, g) Cross-sectional Raman intensity mapping of (f) E_{2g} band and (g) G band of the area shown in (e). Scale bars for (e−g): 10 μm.

To help better evaluate these different structures, Raman mapping of this cross section area was carried out, as shown in Figure 2e−g. A typical Raman spectrum of VACNT-BN is shown in the inset of Figure 2e. For the VACNT-BN region,

DOI: 10.1021/acsanm.8b01727
ACS Appl. Nano Mater. 2019, 2, 100−108

the E_{2g} band was separated from the combined D + E_{2g} band via Lorentzian fitting. As can be seen from the E_{2g} band intensity mapping, which represents the h-BN distribution along the cross section, the top h-BN layer demonstrated a stronger signal than the VACNT-BN section. This was the result of peak shifting caused by the mixing of two materials.[40] As for the G-band intensity mapping, which represents the VACNTs, it proved the existence of VACNTs under the heavy h-BN coating on the surface. A similar analysis was performed on shorter VACNTs as well, and the results were consistent (Figure S8).

Although the above results visually and chemically confirmed that the h-BN was infiltrated inside the VACNT matrices, the combination between every single VACNT and the h-BN shielding layer was yet to be determined. Therefore, we looked further into this matter via various characterization techniques of scanning TEM (STEM). First, from a chemistry point of view, as can be seen in Figure 3b−d, the results of energy dispersive spectroscopy (EDS) for (b) boron, (c) carbon, and (d) nitrogen mapping are presented. The high-angle annular dark field (HAADF) image of the sampled area is shown in Figure 3a as a reference. Strong signals for all three elements were obtained with good contrast. The distribution for both B and N was consistent with C, with no overlapping in the intertube space, indicating that the h-BN was only on the sidewall of the VACNTs. Taking full advantage of the better contrast provided by the HAADF image[41,42] of the sample (Figure 3a), the h-BN coating on VACNT fibers was confirmed. To narrow down the scope and further look into one single VACNT, a HAADF (Figure 3e) image of one single VACNT is shown, alongside the EDS mapping of B (Figure 3f) and N (Figure 3g) as well. As can be seen, a single VACNT was suspended between surrounding structures, and both B and N elements were uniformly covering the VACNT wall.

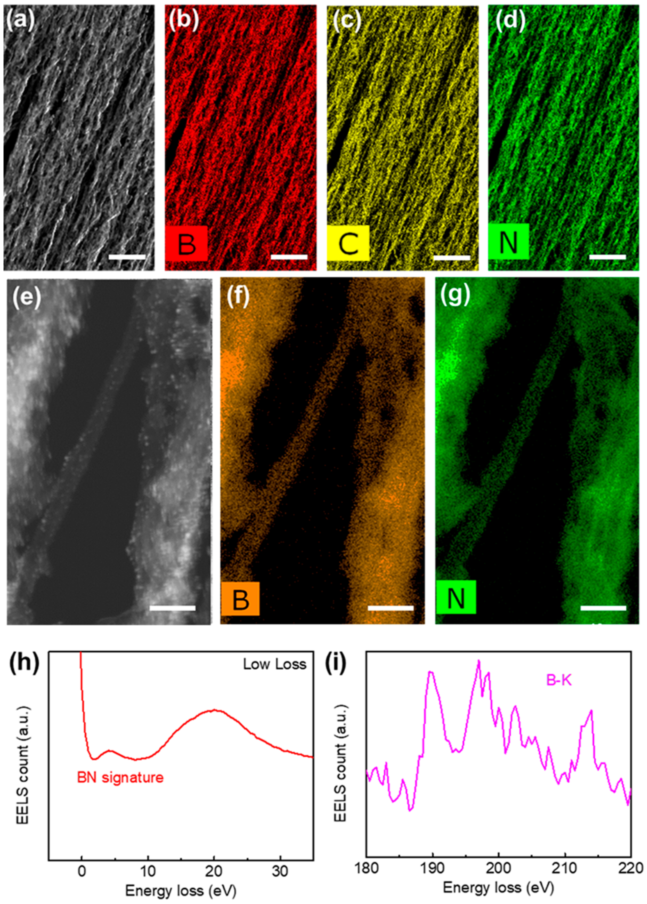

Figure 3. Nanoscale elemental analysis of prepared VACNT-BN nanocomposites. (a) HAADF image, (b) boron, (c) carbon, and (d) nitrogen EDS mapping of VACNT-BN fibers. Scale bars: (a−d) 1 μm. (e) HAADF image, (f) boron, and (g) nitrogen EDS mapping of a single VACNT-BN. Scale bars: (e−g) 40 nm. (h) EELS low loss spectrum of VACNT-BN. (i) BN signature band in EELS spectrum of the VACNT-BN sample.

However, some previous reports suggested that at elevated temperatures C, B, and N can form complex chemical species that are not desired in our study.[43−46] To investigate this matter, EELS of the VACNT-BN sample of a larger area was collected. First, the low loss map of the nanocomposites is shown in Figure 3h, which suggests results consistent with the reported h-BN signature.[47,48] Another set of unique B-K signature peaks that only exist in BN was also identified, as shown in Figure 3i. The full EELS spectrum of the sample and additional features associated with C and N are shown in Figure S9. Interestingly, neither BN nor B−C−N features were identified in the spectrum. These results confidently indicate that the VACNT-BN nanocomposites we fabricated were free of undesired byproducts and were only consist with VACNTs and h-BN.

Furthermore, via close observation, white dots can be distinguished on the VACNT wall, the chemical nature of which, however, could not be determined solely by the HAADF image (Figure 3e). Hence, high-resolution transmission electron microscopy (HRTEM) of a single VACNT (Figure 4a) and VACNT-BN (Figure 4b) were obtained and compared with each other. Compared to a bare VACNT (Figure 4a) with clean walls, lots of additional layered features were identified on the wall of the VACNT-BN (Figure 4b), and the wall of the VACNT-BN is slightly distorted. These features exhibited a similar graphene-like layered structure. To better evidence the existence of the h-BN, we took higher magnification HRTEM images of both VACNT-BN and h-BN film to compare with each other, and the figures have been added in the Supporting Information (Figure S10) and is also shown below. High magnification HRTEM of the outside layers that are suspected to be h-BN is shown in Figure S10a. As can be seen, in addition to the already identified layered structure, the atom−atom distance is roughly measured to be

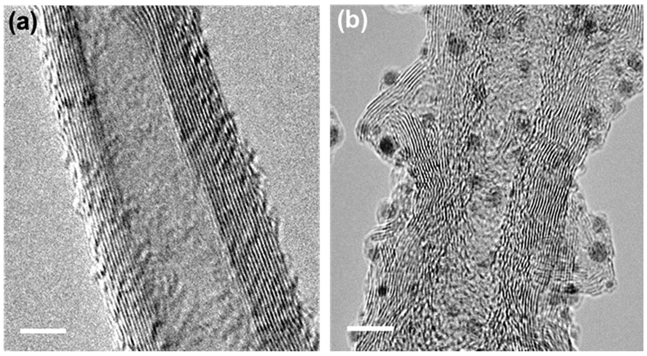

Figure 4. Nanoscale structural analysis of prepared VACNT-BN nanocomposites. HRTEM images of single (a) bare VACNT and (b) VACNT-BN nanocomposites. Scale bars: 5 nm.

2.6 Å, and the distance consisting of two layers is ~5.9 Å. To verify these results, we compared them to the HRTEM of h-BN shown in Figure S10b. It demonstrates a similar graphene-like layered structure, with a layer thickness of roughly 3−4 Å, which is consistent with both shown in Figure 4b and reported results.[30,33,49] Combining this structural consistency and the elemental characterization provided by EELS and EDS, we are therefore positive that these graphene-liked layers outside the VACNT wall are h-BN.[36,39,50,51] In addition, large h-BN nucleation sites were noted (dark round dots). The existence of these large spots is believed to correspond to the white features seen in the HAADF image (Figure 3e). Based on the location of these features, the graphene-like layers were determined to first form by the wall of a VACNT, which served as a template. These layers then served as transition layers for the larger scale nucleation of h-BN dots. This growth mechanism allowed a chemically and structurally stable combination of VACNTs and BN.[36,48] However, as shown in Figure 4b, the wall of VACNT after BN growth has been slightly distorted due to the formation of these BN layers. Compared to other reports with similar CNT-BN structures,[30,52] our results show discontinued BN layers covering the VACNTs instead of a few smooth epitaxial layers. This discontinued formation of BN may have been caused by the purposed nucleation mechanism.

3.3. Electrical Anisotropy. Now that a kind of core−shell structure of the VACNT-BN nanocomposites prepared through our approach was confirmed, we explored its electrical potential performance toward interconnect applications. Two types of VACNT-BN test benches in similar sizes, with orthogonal orientations of VACNTs, were prepared. As can be seen in Figure 5, the top view SEM images of the two test benches were (a) perpendicular to and (b) parallel to the VACNTs' direction, respectively. The insets present the overall view of these two test benches. The test benches were welded onto gold (Au) electrodes in an all-around fashion to ensure good electrical connection. As can be seen in Figure 5a, the VACNTs were pointing downward, and the current passed through the VACNTs horizontally. On the contrary, in Figure 5b, the VACNTs were pointing from left to right, parallel with the direction of the current. Interestingly, the current flowing through these two test benches exhibited a huge difference, of 2 orders of magnitude, in electrical conductivity.

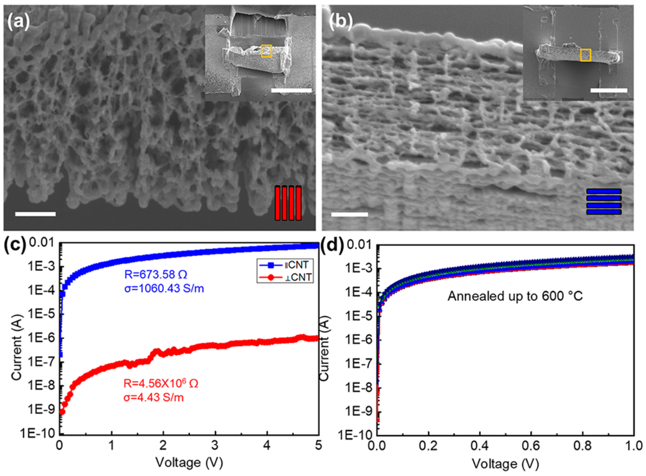

Figure 5. Electrical anisotropy of prepared VACNT-BN nanocomposites. (a, b) VACNT-BN test benches for *I*−*V* analysis where the direction of VACNTs is (a) perpendicular to and (b) parallel to the direction of the current flow. Insets present low magnification SEM images of the test benches. (c) *I*−*V* characteristics in log scale of (a) red and (b) blue. (d) *I*−*V* characteristics of (b) after annealing in argon flow from 100 to 600 °C. Scale bars for (a) and (b): 500 nm. Scale bars for insets of (a, b): 15 μm.

Figure 5c compares the *I*−*V* curves of VACNT-BN measured on both test benches, where the blue and red lines represent the *I*−*V* parallel with the direction of VACNT and perpendicular to the direction of the VACNT, respectively. The electrical conductivity turned out to be 1060.43 S m^{-1} along the VACNT direction, while only 4.43 S m^{-1} measured perpendicular to the VACNT direction. Although the electrical conductivity of the VACNT-BN was significantly lower than bare multiwalled carbon nanotube (MWCNT) bundles, the electrical conductivity of which was reported to be ~2.8 × 10^7 S m^{-1} at a length of ~20 μm,[53] it showed superior electrical conductivity over CNT-polymer mixtures, whose conductivities were usually below 10^{-3} S m^{-1},[21,49] The sample also demonstrated good thermal stability and robust electrical performance after being heat cycled from 100 to 600 °C in argon flow, as shown in Figure 5d, which is significantly beneficial for practical applications. In addition, the red line, representing the current perpendicular to the direction of the VACNTs, showed some nonlinear characteristics. All of these results indicated the existence of different conductive pathways inside the VACNT-BN system.

In an insulator−conductor system, multiple electron percolation thresholds could coexist due to the complex formation of the conducting network.[55] To better understand this phenomenon, the percolation effect of electrons in our VACNT-BN nanocomposites was analyzed. In our VACNT-BN system, the VACNTs were highly oriented and shielded by h-BN layers. Because of the dielectric nature of h-BN compared to the metallic VACNTs, the condition of electron transport was expected to be dominated by the pathways provided by the VACNTs themselves and mainly determined by the geometrical feature of individual VACNTs. Natsuki et al. investigated different electrical percolation behaviors as a result of different orientations and aspect ratios of fillers. Lu et al. compared various simulation works regarding conductive nanocomposites.[51,52] In general, with an increase in aspect ratio, an exponential decrease in the EPT was found, regardless of the waviness of the CNTs.[21,51] As the typical diameter of our sample CNTs was ~20 nm (Figure 4b) and the length of the CNTs in the test benches (Figure 5a,b) was ~20 μm, the aspect ratio was calculated to be 1000:1, which was significantly larger than the ones used in the simulation.[21,51] Consequently, extremely conductive behavior along the direction of the VACNTs is expected.

As for the direction perpendicular to the VACNTs, the introduction of BN on the wall of the VACNTs eliminated the contact between adjacent tubes. The extremely large band gap of BN made it a perfect insulating layer as well. In this case, the intertube conduction of electrons was extremely limited by the high barrier provided, which significantly increased the EPT, resulting in a significantly lower electrical conductivity along this direction. Meanwhile, the electron conduction along the VACNTs was not affected. Overall, VACNTs provided highly aligned electrical conductive pathways while the infiltrated h-BN in the nanocomposites induced the significant difference in EPT along different directions,[50] which comprehensively yielded the highly anisotropic electrical conducting performance of the prepared VACNT-BN nanocomposites.

As a contrast, we also measured the conductivity of bare VACNTs from both the parallel and perpendicular directions (Figure S11) and obtained very similar results although the geometrical aspect ratios were also significantly different for the two directions. It suggests that other factors, besides the geometrical feature of individual VACNTs, take effect in determining the conductive behavior of bare VACNTs. In addition, the physical distortions of VACNTs can affect the electron transport in the CNT,[53] which helps explain the lower electrical conductivity of VACNT-BN (along CNT direction) than bare VACNTs. It was reported that for randomly aligned CNTs measuring direction does not affect conductivity by too much.[20] For the bare VACNTs, multiple contact points actually existed among adjacent tubes. Thus, a complex and nondirectional conducting network formed, on which condition the conduction behavior of the electron was dominated not only by the pathways provided by individual VACNTs but also by the intertube percolation. As a result, no obvious anisotropy in the electrical conducting behaviors was measured for the bare VACNTs.

It can be noticed that the level of electrical conductivity of VACNT-BN comparing with CNTs and other conductive material is substantially lower. In spite of that when comparing to CNT−mixture counterparts, such as CNT−Al_2O_3,[58,59] CNT−MgO,[59] and CNT−Si_3N_4,[60] we still demonstrate competitive electrical conductivity. In our present research, we mainly intend to demonstrate an approach which can effectively infiltrate BN to VACNT forest to improve its thermal stability and electrical anisotropy. Although it is still early to demonstrate an application-ready VACNT-BN system due to the limited absolute electrical conductivity value currently reached, there are possible ways to improve the electrical conductivity in future works, such as (1) reducing the amount of BN in the system. By controlling the amount of the BN infiltrated into the VACNT forest, the insulating layers between tubes will be thinner, and some degree of conduction will be promoted while maintaining good enough anisotropic conducting ability; (2) reducing the growth rate of BN for finer control of BN layers formed outside of the VACNT walls, to avoid discontinuous BN formation and large defects. In addition, avoiding the formation of curvatures of VACNTs could effectively reduce strain in VACNTs, which could increase electron mobility in VACNTs[61] and (3) preparing better quality VACNTs. The quality improvement of bare VACNTs can enhance its electrical conductivity, which should also be able to enhance the electrical conductivity of the corresponding VACNT-BN nanocomposites.

3.4. Thermal Stability.

Previous studies showed moderate thermal stability and reasonable antioxidative ability of VACNTs up until 600 °C.[28,62] Meanwhile, h-BN demonstrated very good antioxidative ability at elevated temperatures.[25] To verify this, the antioxidative stability of our as-grown h-BN film was tested in air. Raman spectra were collected after each oxidation process. As shown in Figure S12a, samples exhibited no evident change as the oxidation temperature increased to even 1100 °C. We further investigated the oxidation temperature dependence of peak position and full width at half-maximum (FWHM) of the E_{2g} peak of h-BN. No obvious change was observed in either FWHM or the peak position, indicating the high quality and high-temperature oxidation resistance of the h-BN films grown by our approach.

The effect of oxidation time on the high-temperature oxidation resistance of the as-grown h-BN films was also studied by treating them at 1100 °C in the air for an extended period (Figure S13). The thickness of the h-BN films was evaluated after each oxidation process via cross-sectional SEM. The original thickness of the h-BN film was ∼11.8 μm (Figure S13a). After being oxidized at 1100 °C for 5 min, the film thickness decreased slightly to ∼11.5 μm (Figure S13b). When the oxidization time was extended to 40 min, the film thickness was decreased to ∼8 μm, suggesting a slow oxidation rate at 1100 °C. In spite of this, the oxidation only happened on the upper section of the layered h-BN, indicating it was a good candidate for the protective layer for the VACNTs.

Although the antioxidative ability of h-BN has been determined, the effect of infiltrating h-BN into VACNT arrays is still unknown. Therefore, we further investigated the antioxidative ability of as-prepared VACNT-BN nanocomposites. The VACNT-BN nanocomposites were first oxidized at 1100 °C for a long treatment time of 40 min in air. Figures S14a and S14b compare the change in sample thickness (a) before and (b) after the high-temperature oxidation treatment. The thickness of the sample decreased by ∼7 μm in total after 40 min of oxidation at 1100 °C. Encouragingly, the oxidation process demonstrated behavior similar to the h-BN layer, which showed that the decrease in thickness only happened in the upper section of the thick h-BN film. Meanwhile, the lower VACNT-BN area was not affected at all. An enlarged SEM image in Figure S14c shows the layered h-BN film near the top surface to be covered with multiple visible rough oxidation sites, suggesting that the oxidation started from the top surface of the h-BN. Scanning electron microscopy images in Figure S14d−f show no visual evidence of oxidation in the original VACNT area, indicating a good protection effect provided by the infiltrated h-BN. The thickness decrease under the high-temperature, oxidation condition in the upper h-BN film was expected and could be improved by increasing the thickness of the upper h-BN further, if needed. It is worthy of noting that during the measurement of electrical conductivity of our VACNT-BN nanocomposites we need to expose the CNT tips to ensure good electrical contact. However, during practical applications, BN will be deposited to cover not only the VACNTs but also the electrical contact and corresponding mating parts, so that its refractory ability and protective effect can be sufficiently utilized.

Because h-BN can be stable up to much higher temperatures, the antioxidative ability of the VACNT-BN nanocomposites was examined under even harsher conditions, including ultrahigh-temperature oxidation treatment (up to 1400 °C) and an ultrahigh-temperature gas erosion test. To better visually observe the oxidation results, VACNT-BN samples in the cuboid pattern, instead of films, were used and oxidized from 1100 to 1400 °C, for 5 min at each temperature, with oxygen partial pressure of 100 mTorr (Figure 6a−d). Magnified SEM images of the top surface are shown in Figure 6e−h, corresponding to Figure 6a−d. As can be seen, the originally smooth surface became rough as the oxidation temperature increased, and significant surface morphology change was observed beginning at 1300 °C (Figure 6g). Meanwhile, the height of each VACNT-BN cuboids started to drastically decrease after 1300 °C (Figure 6i), indicating the loss of VACNTs during the oxidation. It has been reported

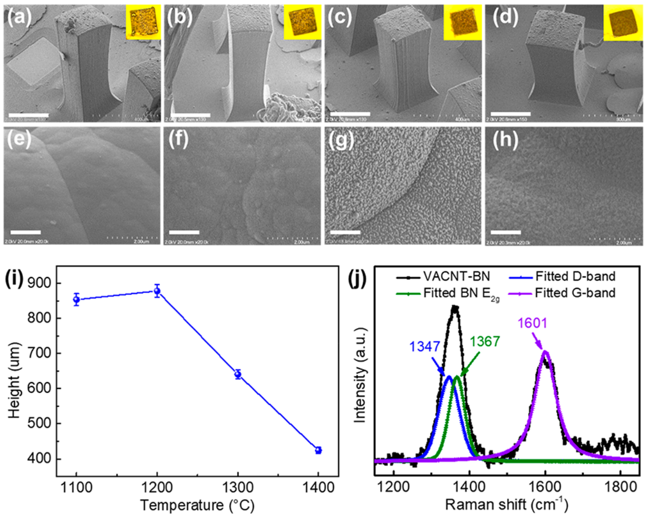

Figure 6. Antioxidative ability of prepared VACNT-BN nanocomposites. (a–d) SEM images of VACNT-BN cuboid samples after oxidation at (a) 1100, (b) 1200, (c) 1300, and (d) 1400 °C. (e–h) Magnified SEM images of the top area of the samples from (a) to (d), respectively. (i) Height change of VACNT-BN cuboid after oxidation. (j) Raman spectrum of VACNT-BN after being oxidized for 30 min at 1400 °C. Fitted lines represent individual peaks of interest.

that h-BN is prone to oxidize under this condition accompanied by a slight weight gain and a decrease in size.[63] The shrinkage of the outside BN caused thinning of the protective BN layer, eventually exposing the inside VACNTs to the environment. In addition, Raman characterization of samples in Figures 6a–d are shown in Figure S15. Compared to the Raman spectrum of the sample before any oxidation treatment (Figure S15a), the combined feature D + E_{2g} around 1370 cm^{-1} demonstrates no significant loss in intensity and a stable peak position. The G-band associated with CNTs, which is around 1580 cm^{-1}, gained slightly change in intensity and became more pronounced after oxidation. The peak position of G-band remained relatively stable after 5 min of oxidation at each temperature. When prolonging the oxidation duration to 30 min at 1400 °C, the G-band blue-shifted to 1601 cm^{-1}. One of the possible reasons for such a blue-shift of the G-band is that the thermal expansion coefficients of CNT (positive) and BN (negative) are mismatched. When heating for a longer time, the BN layers compress the inside CNTs, causing the increase in the Raman shift. Despite this, the overall chemical composition stayed unchanged, which indicates that the outside BN layers can protect the inside VACNTs well at temperature as high as 1400 °C. The result of oxidation of VACNT-BN nanocomposites is a material loss rather than chemical change since carbon and boron do not react to form any side products like B–C–N. Thus, the oxidation cannot be reflected in the Raman spectroscopy. It is this material loss caused by oxidation as well as the shrinkage of BN under oxidative environment which should account for the significant decrease of the height of VACNT-BN nanocomposites after 1300 °C.

An ultrahigh-temperature gas erosion test was performed as well. Figures S16a and S16b show the actual experimental setup and an illustration of the method, respectively. A high-velocity gas flame (2480 sccm) with an ultrahigh temperature (up to 3000 °C) was kept flowing toward the surface of the VACNT-BN sample for 126 min in total. The average height change of the VACNT-BN cuboids on the substrate was estimated by a Zygo NewView optical surface profiler, and the results are shown in Figure S16c. The average height did not change significantly after 126 min of erosion, and the optical images did not show obvious morphology changes either, as shown in the Figure S16c inset. Raman spectra at slightly different stages of the erosion test are shown in Figure S16d. As can be seen, the main features, namely, the D- and G-band for VACNT, as well as the E_{2g} band for h-BN, presented no apparent changes, confirming good erosion resistance of the prepared VACNT-BN nanocomposites against oxygen contained in the ultrahigh temperature, high-velocity gas flow. As a comparison, no on par stability performance for the CNT-polymer-based nanocomposites has been reported as yet. The excellent stability of VACNT-BN as electrical interconnects demonstrates great potential for high-power and high-current density applications, such as insulated-gate bipolar transistors (IGBT).

4. CONCLUSIONS

In summary, a novel approach has been demonstrated for the finely controlled fabrication of refractory VACNT-BN conductive nanocomposites. Ultralong VACNTs (up to 3 mm), as superaligned conducting pathways and building framework templates, were prepared based on which uniformly infiltrated VACNT-BN composite structures were successfully obtained via the one-step CVD process. The as-fabricated VACNT-BN nanocomposites exhibited significant anisotropic electrical conducting performance, excellent thermal stability, and the extraordinary ability to withstand various extreme conditions (e.g., ultrahigh-temperature oxidation and high-velocity hot gas erosion). The h-BN layers which were uniformly infiltrated into the VACNT arrays significantly reduced the intertube electron percolation, providing excellent stability enhancement at the same time. These attributes of VACNT-BN nanocomposites demonstrated great potential to be superior to many CNT-based counterparts for high density interconnect applications. In addition, the CVD process proposed in this work requires minimal complexity and effort in sample preparation, which is promising for the development of a cost-effective, turnkey solution to fabrication of scalable electrical interconnects. Our future work will explore the potential applications for VACNT-BN nanocomposites and their properties under extreme conditions.

■ ASSOCIATED CONTENT

Ⓢ Supporting Information

The Supporting Information is available free of charge on the ACS Publications website at DOI: 10.1021/acsanm.8b01727.

> Figure S1: characterization of grown h-BN films; Figure S2: cross-sectional Raman mapping of grown h-BN film; Figure S3: TEM and EELS characterization of BN grown on SiO_2/Si; Figure S4: XRD spectra of VACNTs, h-BN, and VACNT-BN; Figure S5: morphology characterization of VACNT-BN composite; Figure S6: cross-sectional SEM images of single ultralong VACNT-BN cuboid structure, top to bottom; Figure S7: cross-sectional SEM images of a single ultralong VACNT-BN cuboid structure, side to side; Figure S8: cross-sectional Raman mapping characterization of short VACNT-BN composite; Figure S9: scanning TEM EELS mapping of

VACNT-BN; Figure S10: HRTEM of VACNT-BN and h-BN; Figure S11: electrical conductivity of VACNTs along two different directions; Figure S12: Raman characterization of as-grown BN films after high-temperature oxidation treatments; Figure S13: cross-sectional SEM images of the thick BN film; Figure S14: high-temperature antioxidation ability of VACNT-BN nanocomposites; Figure S15: Raman characterization of VACNT-BN after high-temperature oxidation treatments; Figure S16: ultrahigh-temperature gas erosion test of CNT-BN (PDF)

■ AUTHOR INFORMATION

Corresponding Authors

*E-mail: ylu2@unl.edu.

*E-mail: fanpeixun@gmail.com.

ORCID

Qi Ming Zou: 0000-0002-0414-7435

Da Wei Li: 0000-0001-6967-4968

Lan Jiang: 0000-0003-0488-1987

Yong Feng Lu: 0000-0002-5942-1999

Author Contributions

Q.M.Z. and L.M.D. contributed equally.

Notes

The authors declare no competing financial interest.

■ ACKNOWLEDGMENTS

This research was financially supported by U.S. Department of Energy [NETL: DE-FE0023061] and the Nebraska Center for Energy Science Research. Manufacturing and characterization analyses were performed at the NanoEngineering Research Core Facility (part of the Nebraska Nanoscale Facility), which is partially funded by the Nebraska Research Initiative.

■ REFERENCES

(1) http://www-03.ibm.com/ibm/history/ibm100/us/en/icons/copperchip/.

(2) Bohr, M. T. Interconnect Scaling-the Real Limiter to High Performance ULSI. *Proc. Int. Electron Devices Meet.* **1995**, *95*, 241−244.

(3) Yee, C. F.; Jambek, A. B.; Al-Hadi, A. A. Advantages and Challenges of 10-Gbps Transmission on High-Density Interconnect Boards. *J. Electron. Mater.* **2016**, *45*, 3134−3141.

(4) Holden, H.; Andresakis, J.; Bogatin, E.; Carano, M.; Carpenter, K. A.; Dietz, K. H.; Laing, M.; Vaucher, C.; Viklund, P.; Wuensch, M. *The HDI Handbook*, 1st ed.; El Dorado Hills: 2009.

(5) https://www.ncabgroup.com/hdi-pcb/.

(6) Romero, C.; Park, S.; Kweon, Y.; Park, M. Advanced High Density Interconnection Substrate for Mobile Platform Application. *Proc. Technol. Pap. - Int. Microsystems, Packag. Assem. Circuits Technol. Conf. IMPACT* **2011**, 214−217.

(7) Andricacos, P. C.; Uzoh, C.; Dukovic, J. O.; Horkans, J.; Deligianni, H. Damascene Copper Electroplating for Chip Interconnections. *IBM J. Res. Dev.* **1998**, *42*, 567−574.

(8) Chai, Y.; Chan, P. C. H. H. High Electromigration-Resistant Copper/Carbon Nanotube Composite for Interconnect Application. *IEEE IEDM Technical Digest* **2008**, DOI: 10.1109/IEDM.2008.4796764.

(9) Wei, B. Q.; Vajtai, R.; Ajayan, P. M. Reliability and Current Carrying Capacity of Carbon Nanotubes. *Appl. Phys. Lett.* **2001**, *79*, 1172−1174.

(10) Kim, Y. L.; Li, B.; An, X.; Hahm, M. G.; Chen, L.; Washington, M.; Ajayan, P. M.; Nayak, S. K.; Busnaina, A.; Kar, S.; Jung, Y. J. Highly Aligned Scalable Platinum- Decorated Single-Wall Carbon Nanotube Interconnects. *ACS Nano* **2009**, *3*, 2818−2826.

(11) Kreupl, F.; Graham, A. P. A. P.; Duesberg, G. S. G.; Steinhögl, W.; Liebau, M.; Unger, E.; Hönlein, W. Carbon Nanotubes in Interconnect Applications. *Microelectron. Eng.* **2002**, *64*, 399−408.

(12) Nieuwoudt, A.; Massoud, Y. Evaluating the Impact of Resistance in Carbon Nanotube Bundles for VLSI Interconnect Using Diameter-Dependent Modeling Techniques. *IEEE Trans. Electron Devices* **2006**, *53*, 2460−2466.

(13) Li, J.; Ye, Q.; Cassell, A.; Ng, H. T.; Stevens, R.; Han, J.; Meyyappan, M. Bottom-up Approach for Carbon Nanotube Interconnects. *Appl. Phys. Lett.* **2003**, *82*, 2491−2493.

(14) Homma, Y.; Yamashita, T.; Kobayashi, Y.; Ogino, T. Interconnection of Nanostructures Using Carbon Nanotubes. *Phys. B* **2002**, *323*, 122−123.

(15) Naeemi, A.; Meindl, J. D. Monolayer Metallic Nanotube Interconnects: Promising Candidates for Short Local Interconnects. *IEEE Electron Device Lett.* **2005**, *26*, 544−546.

(16) Sahoo, S.; Chitturi, V. R.; Agarwal, R.; Jiang, J.; Katiyar, R. S. Thermal Conductivity of Freestanding Single Wall Carbon Nanotube Sheet by Raman Spectroscopy. *ACS Appl. Mater. Interfaces* **2014**, *6*, 19958−19965.

(17) Hao, M.; Kumar, A.; Hodson, S. L.; Zemlyanov, D.; He, P.; Fisher, T. S. Brazed Carbon Nanotube Arrays: Decoupling Thermal Conductance and Mechanical Rigidity. *Adv. Mater. Interfaces* **2017**, *4*, 1601042.

(18) Behnam, A.; Guo, J.; Ural, A. Effects of Nanotube Alignment and Measurement Direction on Percolation Resistivity in Single-Walled Carbon Nanotube Films. *J. Appl. Phys.* **2007**, *102*, 044313.

(19) Wu, S. H.; Masaharu, I.; Natsuki, T.; Ni, Q. Q. Electrical Conduction and Percolation Behavior of Carbon Nanotubes/UPR Nanocomposites. *J. Reinf. Plast. Compos.* **2006**, *25*, 1957−1966.

(20) Simoneau, L. P.; Villeneuve, J.; Rochefort, A. Electron Percolation in Realistic Models of Carbon Nanotube Networks. *J. Appl. Phys.* **2015**, *118*, 124309.

(21) Zeng, X.; Xu, X.; Shenai, P. M.; Kovalev, E.; Baudot, C.; Mathews, N.; Zhao, Y. Characteristics of the Electrical Percolation in Carbon Nanotubes/Polymer Nanocomposites. *J. Phys. Chem. C* **2011**, *115*, 21685−21690.

(22) Vigolo, B. An Experimental Approach to the Percolation of Sticky Nanotubes. *Science* **2005**, *309*, 920−924.

(23) Bu, H.; Zhao, M.; Zhang, H.; Wang, X.; Xi, Y.; Wang, Z. Isoelectronic Doping of Graphdiyne with Boron and Nitrogen: Stable Configurations and Band Gap Modification. *J. Phys. Chem. A* **2012**, *116*, 3934−3939.

(24) Zhang, J.; Yang, Y.; Lou, J. Investigation of Hexagonal Boron Nitride as an Atomically Thin Corrosion Passivation Coating in Aqueous Solution. *Nanotechnology* **2016**, *27*, 364004.

(25) Kostoglou, N.; Polychronopoulou, K.; Rebholz, C. Thermal and Chemical Stability of Hexagonal Boron Nitride (h-BN) Nanoplatelets. *Vacuum* **2015**, *112*, 42−45.

(26) Cassabois, G.; Valvin, P.; Gil, B. Hexagonal Boron Nitride Is an Indirect Bandgap Semiconductor. *Nat. Photonics* **2016**, *10*, 262−266.

(27) Li, W. Z.; Wen, J. G.; Sennett, M.; Ren, Z. F. Clean Double-Walled Carbon Nanotubes Synthesized by CVD. *Chem. Phys. Lett.* **2003**, *368*, 299−306.

(28) Zou, Q. M.; Deng, L. M.; Li, D. W.; Zhou, Y. S.; Golgir, H. R.; Keramatnejad, K.; Fan, L. S.; Jiang, L.; Silvain, J. F.; Lu, Y. F. Thermally Stable and Electrically Conductive, Vertically Aligned Carbon Nanotube/Silicon Infiltrated Composite Structures for High-Temperature Electrodes. *ACS Appl. Mater. Interfaces* **2017**, *9*, 37340−37349.

(29) Jing, L.; Tay, R. Y.; Li, H.; Tsang, S. H.; Huang, J.; Tan, D.; Zhang, B.; Teo, E. H. T.; Tok, A. I. Y. Coaxial Carbon@boron Nitride Nanotube Arrays with Enhanced Thermal Stability and Compressive Mechanical Properties. *Nanoscale* **2016**, *8*, 11114−11122.

(30) Jing, L.; Samani, M. K.; Liu, B.; Li, H.; Tay, R. Y.; Tsang, S. H.; Cometto, O.; Nylander, A.; Liu, J.; Teo, E. H. T.; Tok, A. I. Y. Thermal Conductivity Enhancement of Coaxial Carbon@Boron

Nitride Nanotube Arrays. *ACS Appl. Mater. Interfaces* **2017**, *9*, 14555−14560.

(31) Stano, K. L.; Carroll, M.; Padbury, R.; McCord, M.; Jur, J. S.; Bradford, P. D. Conformal Atomic Layer Deposition of Alumina on Millimeter Tall, Vertically-Aligned Carbon Nanotube Arrays. *ACS Appl. Mater. Interfaces* **2014**, *6*, 19135−19143.

(32) Pierson, H. O. Boron Nitride Composites By Chemical Vapor Deposition. *J. Compos. Mater.* **1975**, *9*, 228−240.

(33) Li, L. H.; Chen, Y. Atomically Thin Boron Nitride: Unique Properties and Applications. *Adv. Funct. Mater.* **2016**, *26*, 2594−2608.

(34) Zhi, C.; Bando, Y.; Tang, C.; Kuwahara, H.; Golberg, D. Large-Scale Fabrication of Boron Nitride Nanosheets and Their Utilization in Polymeric Composites with Improved Thermal and Mechanical Properties. *Adv. Mater.* **2009**, *21*, 2889−2893.

(35) Xue, Y.; Liu, Q.; He, G.; Xu, K.; Jiang, L.; Hu, X.; Hu, J. Excellent Electrical Conductivity of the Exfoliated and Fluorinated Hexagonal Boron Nitride Nanosheets. *Nanoscale Res. Lett.* **2013**, *8*, 49.

(36) Arenal, R.; Lopez-Bezanilla, A. In-Situ Formation of Carbon Nanotubes Encapsulated within Boron Nitride Nanotubes via Electron Irradiation. *ACS Nano* **2014**, *8*, 8419−8425.

(37) Zhang, G.; Zhou, R.; Zeng, X. C. Carbon Nanotube and Boron Nitride Nanotube Hosted C60−V Nanopeapods. *J. Mater. Chem. C* **2013**, *1*, 4518−4526.

(38) An, W.; Turner, C. H. Linking Carbon and Boron-Nitride Nanotubes: Heterojunction Energetics and Band Gap Tuning. *J. Phys. Chem. Lett.* **2010**, *1*, 2269−2273.

(39) Walker, K. E.; Rance, G. A.; Pekker, Á.; Tóháti, H. M.; Fay, M. W.; Lodge, R. W.; Stoppiello, C. T.; Kamarás, K.; Khlobystov, A. N. Growth of Carbon Nanotubes inside Boron Nitride Nanotubes by Coalescence of Fullerenes: Toward the World's Smallest Coaxial Cable. *Small Methods* **2017**, *1*, 1700184.

(40) Miranda, A. M.; Castilho-Almeida, E. W.; Martins Ferreira, E. H.; Moreira, G. F.; Achete, C. A.; Armond, R. A. S. Z.; Dos Santos, H. F.; Jorio, A. Line Shape Analysis of the Raman Spectra from Pure and Mixed Biofuels Esters Compounds. *Fuel* **2014**, *115*, 118−125.

(41) Jesson, D. E.; Pennycook, S. J. Incoherent Im Aging of Crystals Using Therm Ally Scattered Electrons. *Proc. R. Soc. London, Ser. A* **1995**, *449*, 273−293.

(42) Mehrtens, T.; Schowalter, M.; Tytko, D.; Choi, P.; Raabe, D.; Hoffmann, L.; Jönen, H.; Rossow, U.; Hangleiter, A.; Rosenauer, A. Measuring Composition in InGaN from HAADF-STEM Images and Studying the Temperature Dependence of Z-Contrast. *J. Phys.: Conf. Ser.* **2013**, *471*, 012009.

(43) Wang, J.; Hao, J.; Liu, D.; Qin, S.; Portehault, D.; Li, Y.; Chen, Y.; Lei, W. Porous Boron Carbon Nitride Nanosheets as Efficient Metal-Free Catalysts for the Oxygen Reduction Reaction in Both Alkaline and Acidic Solutions. *ACS Energy Lett.* **2017**, *2*, 306−312.

(44) Lei, W.; Portehault, D.; Dimova, R.; Antonietti, M. Boron Carbon Nitride Nanostructures from Salt Melts: Tunable Water-Soluble Phosphors. *J. Am. Chem. Soc.* **2011**, *133*, 7121−7127.

(45) Kosaka, M.; Urakami, N.; Hashimoto, Y. Formation of Graphitic Carbon Nitride and Boron Carbon Nitride Film on Sapphire Substrate. *Jpn. J. Appl. Phys.* **2018**, *57*, 02CB09.

(46) Yap, Y. K. *B-C-N Nanotubes and Related Nanostructures*; Springer-Verlag: Berlin, Germany, 2009.

(47) Dobigeon, N.; Brun, N. Ultramicroscopy Spectral Mixture Analysis of EELS Spectrum-Images. *Ultramicroscopy* **2012**, *120*, 25−34.

(48) Cretu, O.; Lin, Y. C.; Koshino, M.; Tizei, L. H. G.; Liu, Z.; Suenaga, K. Structure and Local Chemical Properties of Boron-Terminated Tetravacancies in Hexagonal Boron Nitride. *Phys. Rev. Lett.* **2015**, *114*, 075502.

(49) Nag, A.; Raidongia, K.; Hembram, K. P. S. S.; Datta, R.; Waghmare, U. V.; Rao, C. N. R. Graphene Analogues of BN: Novel Synthesis and Properties. *ACS Nano* **2010**, *4*, 1539−1544.

(50) Yun, J.; Oh, H.; Jo, J.; Hwi Lee, H.; Kim, M.; Yi, G.-C. Selective-Area Heteroepitaxial Growth of h -BN Micropatterns on Graphene Layers. *2D Mater.* **2018**, *5*, 015021.

(51) Yasuda, A.; Kawase, N.; Banhart, F.; Mizutani, W.; Shimizu, T.; Tokumoto, H. Graphitization Mechanism during the Carbon-Nanotube Formation Based on the in-Situ HRTEM Observation. *J. Phys. Chem. B* **2002**, *106*, 1849−1852.

(52) Chang, H.; Tsai, H.; Lin, W.; Chu, Y.; Hsu, W. Hexagonal Boron Nitride Coated Carbon Nanotubes: Interlayer Polarization Improved Field Emission. *ACS Appl. Mater. Interfaces* **2015**, *7*, 14456−14462.

(53) Lekawa-Raus, A.; Patmore, J.; Kurzepa, L.; Bulmer, J.; Koziol, K. Electrical Properties of Carbon Nanotube Based Fibers and Their Future Use in Electrical Wiring. *Adv. Funct. Mater.* **2014**, *24*, 3661−3682.

(54) McClory, C.; McNally, T.; Baxendale, M.; Potschke, P.; Blau, W.; Ruether, M. Electrical and Rheological Percolation of PMMA/MWCNT Nanocomposites as a Function of CNT Geometry and Functionality. *Eur. Polym. J.* **2010**, *46*, 854−868.

(55) Kovacs, J. Z.; Velagala, B. S.; Schulte, K.; Bauhofer, W. Two Percolation Thresholds in Carbon Nanotube Epoxy Composites. *Compos. Sci. Technol.* **2007**, *67*, 922−928.

(56) Lu, W.; Chou, T. W.; Thostenson, E. T. A Three-Dimensional Model of Electrical Percolation Thresholds in Carbon Nanotube-Based Composites. *Appl. Phys. Lett.* **2010**, *96*, 223106.

(57) Natsuki, T.; Endo, M.; Takahashi, T. Percolation Study of Orientated Short-Fiber Composites by a Continuum Model. *Phys. A* **2005**, *352*, 498−508.

(58) Inam, F.; Yan, H.; Jayaseelan, D. D.; Peijs, T.; Reece, M. J. Electrically Conductive Alumina-Carbon Nanocomposites Prepared by Spark Plasma Sintering. *J. Eur. Ceram. Soc.* **2010**, *30*, 153−157.

(59) Flahaut, E.; Peigney, A.; Laurent, C.; Marlière, C.; Chastel, F.; Rousset, A. Carbon Nanotube-Metal-Oxide Nanocomposites: Microstructure, Electrical Conductivity and Mechanical Properties. *Acta Mater.* **2000**, *48*, 3803−3812.

(60) Balázsi, C.; Kónya, Z.; Wéber, F.; Biró, L. P.; Arató, P. Preparation and Characterization of Carbon Nanotube Reinforced Silicon Nitride Composites. *Mater. Sci. Eng., C* **2003**, *23*, 1133−1137.

(61) Hirai, H.; Ogawa, M.; Souma, S. Effect of Strain on Electron Mobility in Graphene. *IEEE SISPAD* **2017**, 209−212.

(62) Frank, B.; Rinaldi, A.; Blume, R.; Schlögl, R.; Su, D. S. Oxidation Stability of Multiwalled Carbon Nanotubes for Catalytic Applications. *Chem. Mater.* **2010**, *22*, 4462−4470.

(63) Jacobson, N.; Farmer, S.; Lavrenko, V. A.; Alexeev, A. F. High-Temperature Oxidation of Boron Nitride. *Ceram. Int.* **1986**, *12*, 25−31.